Research article

Pilar Gomez-Rodriguez, Esther Soria, Yu Jin, Andrés Caño, Irene Llorente, Alexander Cuadrado, Antonio Mariscal-Jiménez, Amanda K. Petford-Long, Rosalía Serna and José Gonzalo*

Toward white light emission from plasmonic-luminescent hybrid nanostructures

Abstract: We study the light emission of plasmonic-luminescent hybrid nanostructures consisting of Ag nanoparticles (NPs) embedded in europium oxide (EuO_X). The Ag NPs present a bidimensional organization in the nanostructures and they optically behave as oblate spheroids. The photoluminescence (PL) spectral response of the nanostructures evolves from a narrow red emission characteristic of Eu^{3+} ions in absence of Ag NPs to a broad blue-green emission band associated with Eu^{2+} ions when the layer of Ag NPs is present. This behavior is not related to a change in the Eu^{2+}/Eu^{3+} ratio, which is verified by compositional analysis. Instead, a detailed investigation of the PL emission of the nanostructures suggests that the coupling of the Ag NPs to the Eu^{2+} ions present in the EuO_X layer, which manifests itself in an efficient sensitization of these ions, enhances their broad visible emission. In particular, the longitudinal mode of the Ag NPs surface plasmon is considered to be responsible for the efficient energy transfer for the non-normal incidence excitation PL configuration used. Finally, the use of a capping amorphous Al_2O_3 layer allows improving the robustness of

hybrid nanostructures and further enhances their PL emission. These findings provide a new path to actively control the selective excitation of Eu^{2+} and Eu^{3+} ions via a controlled coupling with the surface plasmon resonance modes of the Ag NPs and points to these nanostructures as promising building blocks for the development of integrable white light sources.

1 Introduction

White light-light-emitting diodes (WL-LEDs) have almost completely replaced conventional lighting sources due to their high lifetime, superior efficiency, energy-saving, and safety. Nevertheless, current commercial technology based on a blue LED combined with a YAG:Ce phosphor embedded in an epoxy resin coating presents limitations due to a red color deficiency and thermal constraints that may affect light emission and limit the applicability of WL-LEDs [1–6]. Among the alternatives to produce WL-LEDs, a usual approach consists of the combination of UV or blue excitation sources with different rare-earth-doped amorphous or crystalline phosphors [7] that emit light in the blue, green, and red wavelength ranges in order to obtain white light by their combination [1, 2, 6]. However, the use of different phosphors decreases the efficiency of the device and presents technical problems associated with the combination of phosphors with different excitation requirements and physical and chemical properties. Thus, the use of light-emitting nanostructures [8] based on a single rare-earth-based phosphor capable of transforming the excitation light into white light is an appealing alternative [2, 9, 10]. For that purpose, an appropriate good absorption in the UV-Blue wavelength range, strong chemical and oxygen stability, along with a high conversion efficiency are required [1, 5].

*Corresponding author: José Gonzalo, Laser Processing Group, Instituto de Optica, IO-CSIC, Serrano 121, Madrid 28006, Spain, E-mail: j.gonzalo@csic.es. https://orcid.org/0000-0001-5523-2640
Pilar Gomez-Rodriguez, Esther Soria, Andrés Caño, Antonio Mariscal-Jiménez and Rosalía Serna, Laser Processing Group, Instituto de Optica, IO-CSIC, Serrano 121, Madrid 28006, Spain
Yu Jin and Amanda K. Petford-Long, Materials Science and Engineering, Northwestern University, 2220 Campus Drive, Evanston 60208-0001, IL, USA; and Materials Science Division, Argonne National Laboratory, 9700 S Cass Avenue, Lemont, IL 60439, USA
Irene Llorente, Centro Nacional de Investigaciones Metalúrgicas, CENIM-CSIC, Avda. Gregorio del Amo 8, Madrid 28040, Spain
Alexander Cuadrado, Universidad Rey Juan Carlos, Escuela Superior de Ciencias Experimentales y Tecnología, Móstoles, Madrid 28933, Spain

In particular, Europium is attracting increasing attention for WL-LEDs due to its unique properties [3, 9–12]. Eu forms two different stable oxides, europium sesquioxide (Eu$_2$O$_3$), which is a wide bandgap oxide, and europium monoxide (EuO), a ferromagnetic semiconductor [13, 14]. The photoluminescence (PL) response of europium mainly originates from its 4f electrons and it depends strongly on the valence state of the Eu [9, 11, 15]. Eu^{2+} presents a short lifetime, very broad emission PL band originated from the dipole-allowed $4f^6 5d \rightarrow 4f^7$ transitions that covers the 450–600 nm spectral region [3, 9, 11, 15–17], and is highly sensitive on the host [1, 3]. On the contrary, Eu^{3+} presents a high purity red emission with a long lifetime, associated with the dipole-forbidden intra-4f shell $^5D_0 \rightarrow {}^7F_2$ transition that is observed at 612 nm in the case of cubic Eu$_2$O$_3$ [2, 11, 18–20]. This emission is much less dependent on the host than that of Eu^{2+}, which converts Eu^{3+} to a powerful activator of the red color. Yet, Eu^{3+} emission can be slightly tuned in the red spectral region by modifying the crystalline field around the ions, such as for instance by changing the crystalline phase from cubic to monoclinic [18] or the stress conditions of the host [4, 6]. Thus, a combination of both oxidation states, Eu^{2+} and Eu^{3+}, in the same matrix is appealing when considering WL-LEDs applications, as white light emission could be achieved using a single Eu-based phosphor [10, 16]. Unfortunately, Eu^{3+} presents a small absorption cross-section in the UV range due to the dipole-forbidden nature of the intra-4f shell transitions, which is not desirable for their applicability. Thus, their PL performance must be enhanced for practical applications.

A promising approach is to sensitize Eu ions with other dopants, such as Ag, as it has been found that Ag species may promote Eu excitation by different mechanisms. In this context, the increase of Eu^{3+} luminescence has been related to either plasmonic effects associated with the enhancement of the electromagnetic field in the vicinity of Ag NPs when the excitation wavelength is in the range of the surface plasmon resonance (SPR) of the NPs [19, 21–23], or to energy transfer (ET) processes between the Eu ions and Ag$^+$ ions [19] or small Ag clusters not showing SPR (Ag NCs) [24–26]. The dominant excitation mechanism has been found to be strongly related to the preparation method and type of matrix in which Eu and Ag are embedded [19, 24]. However, these methods must be compatible with microelectronic technologies required for the fabrication of the UV or blue excitation sources. In particular, Pulsed Laser Deposition (PLD) is very suitable for the synthesis of phosphor materials for WL-LED applications, as it allows not only good quality conformal surface covering [27] but also the synthesis of tailored nanostructures containing metal NPs [28, 29]. PLD has

been successfully applied to the synthesis of Eu$_2$O$_3$ [18, 30] and EuO films [13, 31, 32], and recently, we synthesized stable nanocrystalline EuO$_x$ films, whose PL emission could be tuned through control of the Eu^{2+}/Eu^{3+} ratio by varying the deposition parameters, to obtain either red or blue-green emission associated to Eu^{3+} and Eu^{2+}, respectively [15]. The aim of this work is to contribute to the development of white light-emitting integrated platforms. We first exploit the capabilities of PLD to produce in a single step hybrid plasmonic-luminescent nanostructures consisting of EuO$_x$ with an underlayer of Ag NPs, which leads to a blue-green emission due to the simultaneous emission from Eu^{2+} and Eu^{3+} ions, and then, we discuss the mechanisms responsible for the observed broadband visible light emission.

2 Materials and methods

2.1 Nanostructure fabrication

Plasmonic-luminescent (Pl-L) hybrid nanostructures consisting of europium oxide (EuO$_x$) and Ag nanoparticles (Ag NPs) were prepared by alternate pulsed laser deposition (PLD) using an ArF excimer laser (λ = 193 nm; 20 ns pulse duration; energy density = 3.5 J cm^{-2}) inside a vacuum chamber (Pressure: $2 \pm 1 \times 10^{-4}$ Pa), equipped with a multi-target holder. Three different targets were used: Sintered Al$_2$O$_3$ (99.99%), Monoclinic Eu$_2$O$_3$ (99.99%), and Ag. During the deposition process, both substrate and target holders were rotated continuously to achieve homogenous thin films and to avoid crater formation, respectively. The nanostructures were deposited at room temperature on (100) silicon substrates ultrasonically cleaned in acetone (99.0%) and ethanol (99.9%) in a single step. First, we deposited an amorphous Al$_2$O$_3$ (a-Al$_2$O$_3$) layer, on top of which we grew a single layer of Ag NPs by taking advantage of the Volmer-Weber nucleation process of a metal layer on the a-Al$_2$O$_3$ dielectric surface. Then, we deposited EuO$_X$ to first fill the space between Ag NPs and then to completely cover them with a EuO$_X$ layer. Finally, we protected in some cases the EuO$_X$ layer with an additional a-Al$_2$O$_3$ capping layer. More details on the deposition sequence are described elsewhere [33, 34]. Nanostructures having the configurations shown in Figure 1 were produced: EuO$_X$ films containing a layer of Ag NPs (Ag NPs:EuO$_X$) deposited on an a-Al$_2$O$_3$ buffer layer (uncapped, Figure 1A), and Ag NPs:EuO$_X$ films sandwiched between a-Al$_2$O$_3$ buffer and capping layers (capped, Figure 1B). In addition, EuO$_X$ (Figure 1C) and Ag NPs:Al$_2$O$_3$ (Figure 1D) references were produced. Both buffer and capping Al$_2$O$_3$ layers were set to be 10 nm thick, while the thickness of the EuO$_X$ layer was designed to be in the range of 10–30 nm. In order to apply different annealing treatments on identical films, four samples were produced simultaneously on 0.5 $\times$ 0.5 cm^2 silicon substrates for each nanostructure configuration. One of them was kept at room temperature (As-deposited), while the others were step-annealed in air up to 150 °C, 200 °C, and 300 °C, respectively. The temperature rise rate was 10 °C/min and the annealing time was 1 h at each temperature.

2.2 Characterization and measurements

Transmission electron microscopy (TEM) in a JEOL 2100F instrument operated at 200 kV was used for structural characterization of both plan-view and cross-section samples. Plan-view samples were prepared by direct deposition of the Pl-L hybrid nanostructures on carbon-coated mica (C-mica) substrates at room temperature. Once deposited, the samples were floated off in deionized water and picked up on copper grids for observation. Cross-section samples were made by focused ion beam milling (Zeiss NVision) from nanostructures deposited on Si substrates and coated with a gold layer for protection from beam damage. The composition distribution of the cross-section samples was characterized by scanning TEM (STEM) EDS mapping (FEI Talos F200X). The chemical composition of the Pl-L hybrid nanostructures and Eu oxidation state was characterized by X-ray photoelectron spectroscopy (XPS). XPS analysis was performed using a hemispherical electron analyzer (CLAM2) with Al $K\alpha$ (300 W power) source. The background vacuum in the chamber was ~10^{-5} Pa during data acquisition. Spectra resolution was 20 eV of Pass Energy, which is typical for high-resolution conditions. XPS spectra were analyzed using CasaXPS software. Finally, the formation of crystalline phases was determined by X-ray Diffraction (XRD) (D8 Advance, Bruker, Germany) with Cu $K\alpha$ radiation.

Optical characterization of the nanostructures was performed through reflectance spectroscopy using a Woollam VASE ellipsometer (Woollam Co. Inc.) set in photometry mode. The light was generated by a white light source (Xe lamp), filtered spectrally by a single monochromator. Then, the light was collimated and passed through a polarizer to generate either s- or p-linear polarization for the incident light beam. The angle of incidence (AOI) was 55° and the reflected light was detected by a silicon detector. PL emission of the Pl-L hybrid nanostructures was measured under excitation at λ = 355 nm (P = 145 mW) from a Genesis CX 355-200 optically pumped semiconductor continuous-wave laser (Coherent) using a lens with a focal distance of f = 150 nm, incident at an angle δ = 55° onto the sample. The luminescence emitted by the films was collected in the normal direction to their surface with a ×10, NA = 0.26 Mitutoyo objective and imaged by means of a tube lens with f = 100 mm onto a 2 mm slit of a Czerny–Turner type monochromator (ActonSpectraPro300i, diffraction grating = 1200 g/mm (VIS)) and detected through a photomultiplier (EMI9659QB-S20). The spectral resolution
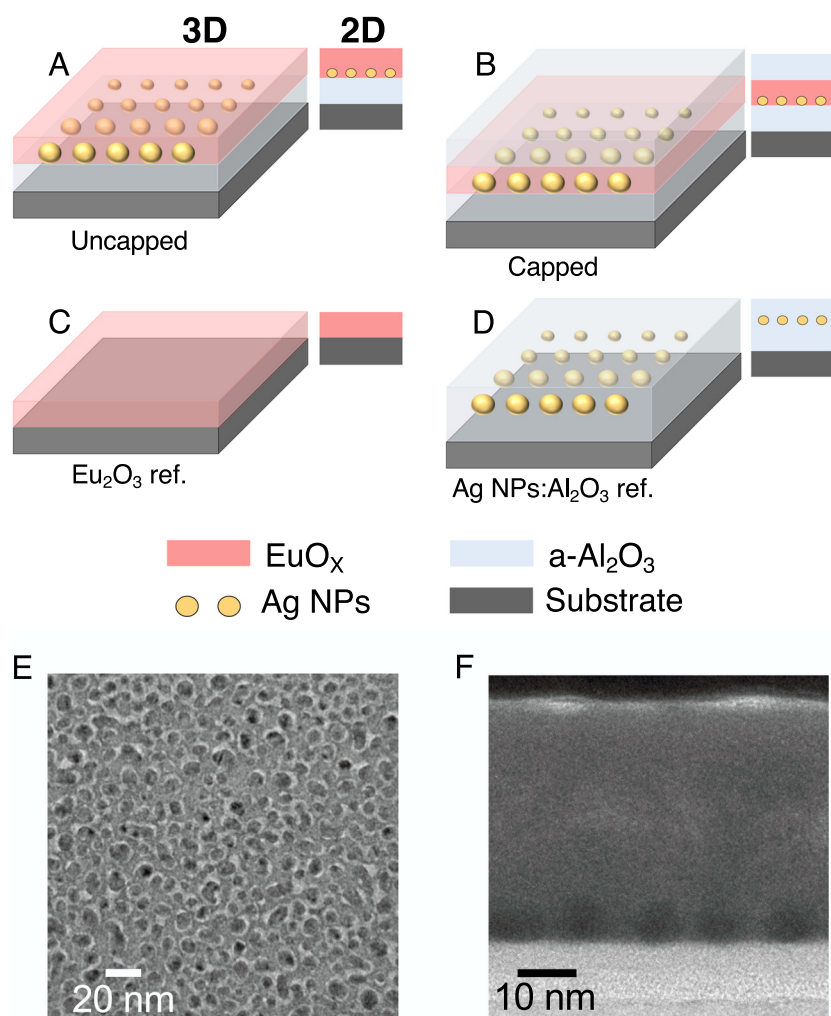

Figure 1: Schematic representation of the Ag NPs:EuO$_x$ Pl-L hybrid nanostructures and references: (A) Uncapped Ag NPs:EuO$_x$ on a-Al$_2$O$_3$ buffer layer; (B) Capped Ag NPs:EuO$_x$ sandwiched between buffer and capping a-Al$_2$O$_3$ layers; (C) EuO$_x$ reference, and (D) Ag NPs:Al$_2$O$_3$ reference. (E) Plan-view and (F) Cross-section TEM images of uncapped Ag NPs:EuO$_x$ Pl-L hybrid nanostructures deposited on C-mica and Si substrates, respectively.

was 2 nm. The signal was amplified using a standard lock-in technique employing an optical chopper and collected by a PC. All PL spectra were recorded at room temperature.

3 Results and discussion

3.1 Ag NPs:EuO$_X$ Pl-L hybrid nanostructures

Figure 1E shows a plan-view bright-field TEM image of an uncapped as-deposited Ag NPs:EuO$_X$ Pl-L hybrid nanostructure with a nominal 30 nm thick EuO$_X$ layer (schematic uncapped in Figure 1A). We can clearly appreciate Ag NPs that are uniformly distributed across the sample; however, the contrast difference between EuO$_X$-covered Ag NPs and EuO$_X$ areas is limited due to the low mass difference between Ag and Eu. Thus, we have considered a representative Ag NPs:Al$_2$O$_3$ reference to analyze the morphology, size, and organization of the Ag NPs as described in Supplementary Material S1. NPs present a circular or slightly elliptical in-plane projected shape with an average length and breadth of 10.9 ± 4.3 nm and 7.6 ± 2.3 nm, respectively, whereas the average spacing between NPs is 11.2 ± 1.9 nm. The measured NP density is 5.2×10^3 NPs µm^{-2} and the surface coverage is close to 40%. Figure 1F shows a cross-section TEM image corresponding to an uncapped Ag NPs:EuO$_X$ nanostructure. Ag NPs (circular darkest contrast regions) are embedded between two regions that correspond to the buffer a-Al$_2$O$_3$ layer (lightest contrast) and the EuO$_X$ layer (dark contrast). Thermal annealing of EuO$_X$ films has been found to improve their PL response [20]. However, the melting temperature of the NPs depends on their characteristic size. Experimental melting values in the range from ≈115 to 530 °C that are lower than the melting temperature of bulk Ag (T$_m$(Ag) = 962 °C), have been reported in the case of Ag NPs with a diameter in the range of a few to 20 nm, such as those shown in Figure 1 [35, 36]. We have estimated a melting temperature of ≈420 ± 50 °C for substrate-supported Ag NPs with a characteristic diameter of 9.2 nm using the Gibbs–Thomson equation as described in Supplementary Material S2. Moreover, the studied Ag NPs are embedded in an oxide layer, which improves their thermal stability [37], and thus, the calculated melting temperature of Ag NPs is likely a lower estimation. The stability of the nanostructures upon annealing has been further confirmed by optical measurements using ellipsometric analysis of as-deposited and step-annealed up to 300 °C uncapped Ag NPs:EuO$_X$ hybrid nanostructures (Supplementary Material S2). The extinction coefficient (k) obtained from numerical inversion from the ellipsometric data (ψ and Δ) that is presented in

Supplementary Material Figure S3C is very similar for as-deposited and annealed structures, i.e. the optical properties related to the Ag NPs are not altered by the annealing. This result indicates that the Ag NPs size and their size distribution undergo very limited changes upon annealing. Therefore, we will consider in the following the morphological analysis of the as-deposited nanostructures to be representative of the annealed ones.

STEM EDS analysis allows a detailed study of the distribution of Ag NPs within the nanostructures. Figure 2A shows the STEM high-angle annular dark-field (HAADF) corresponding to the cross-section TEM sample presented in Figure 1F, and the STEM-EDS composition map images corresponding to Si, O, Al, Ag, and Eu. We have determined the in-depth distribution of these elements by averaging the data across the horizontal direction in Figure 2A (i.e., parallel to the substrate surface) and the obtained EDS composition profiles along the nanostructure normal from the Si substrate to the top EuO$_X$ layer (small to large thickness values) are shown in Figure 2B. Si and O composition profiles evidence the presence of a native SiO$_X$ layer a few nm thick on top of the Si substrate. The intensity profile for Al shows the main peak corresponding to the buffer Al$_2$O$_3$ layer located above the SiO$_X$ (≈20–28 nm thickness range) as well as a small Al peak overlapping with the SiO$_X$ layer, which is likely related to the implantation of a small fraction of Al species into the SiO$_X$ layer during the deposition process. At a higher thickness range, we observe the Ag (≈25–33 nm) and Eu (>24 nm) peaks that correspond to the Ag NPs and the EuO$_X$ layer. As it is shown in Figure 1E, the bottom part of the Eu and Ag peaks overlap. This is due to the fact that Ag NPs do not form a continuous layer and EuO$_X$ fills the area in between the Ag NPs.

In order to determine the thickness of the different layers from the composition profiles we must have in mind that the element distribution is not a square-wave distribution, but it is closer to a Gaussian distribution, such as those plotted in Figure 2B for Ag and Al, due to spreading associated to the X-ray diffraction limit. Thus, we have estimated the thickness of each layer by averaging the FWHM and the 1/e width of each line profile shown in Figure 2B [38]. The calculated thicknesses of the a-Al$_2$O$_3$ buffer and EuO$_X$ layers are (Th$_{Al2O3}$ = 5.5 ± 1.0 nm, and Th$_{EuOx}$ = 31.5 ± 1.0 nm, respectively, whereas the height of the Ag NPs is estimated to be H$_{AgNPs}$ = 5.5 ± 1.5 nm. The values obtained both for Ag NPs and the EuO$_X$ layers are in good agreement with the nominal ones. However, the a-Al$_2$O$_3$ buffer layer is thinner than intended, which is most likely related to the implantation into the substrate of a fraction of the arriving Al atoms and ions during the
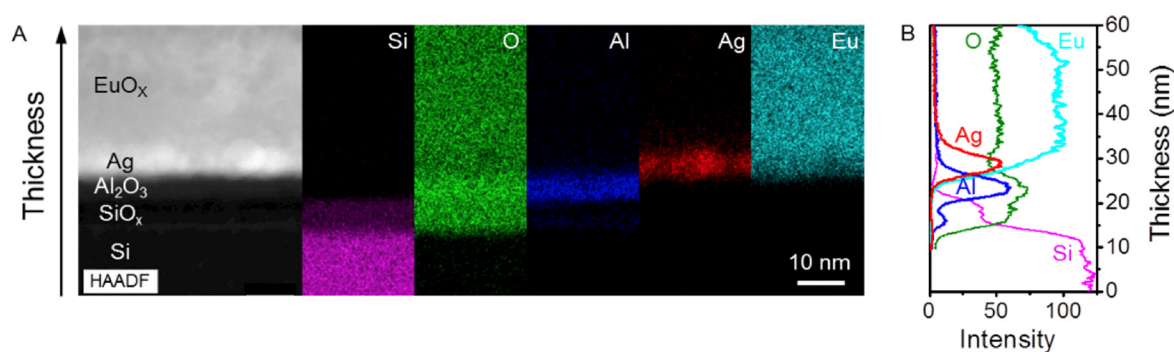
Figure 2: (A) Cross-section HAADF image, and STEM-EDS composition map images corresponding to Si, O, Al, Ag and Eu obtained for the uncapped Ag NPs:EuO$_X$ Pl-L hybrid nanostructure shown in Figure 1F. (B) EDS line profiles for Si, O, Al, Ag, and Eu along the nanostructure normal from the Si substrate to the top EuO$_X$ layer.

deposition process as evidenced in Figure 2B. In addition, we observe a region of ≈1.0–1.5 nm at the SiO$_2$/Al$_2$O$_3$ and Al$_2$O$_3$/Ag-NPs:EuO$_X$ interfaces where the EDS line profiles of the elements of the different layers overlap; thus suggesting a possible mixing. The STEM probe size is ~0.2 nm, though the spatial resolution of the EDS maps could be greater than 1 nm depending on the sample thickness, which could partly explain the observed overlapping. However, the degree of mixing is very small and, as is evidenced by Figures 1F and 2A, we have a well-defined nanostructure consisting of a layer of Ag NPs that lies on an a-Al$_2$O$_3$ buffer layer that is covered by a EuO$_X$ layer. Finally, there is no evidence of the presence of Ag in the EuO$_X$ layer covering the Ag NPs.

High-resolution XPS spectra were recorded to analyze the Eu 3d and Eu 4d core-level peaks in order to investigate the oxidation states of Eu ions. Figure 3A compares the Eu 3d core-level XPS spectra corresponding to as-deposited and step-annealed up to 300 °C 30 nm thick EuO$_X$ references, and an uncapped Pl-L hybrid nanostructure step-annealed up to 300 °C. Photoemission spectra show a similar shape with four emission bands. Those centered at 1135 and 1164 eV correspond to the trivalent doublet, Eu^{3+} 3$d_{5/2}$ and 3$d_{3/2}$, formed by the components due to the spin–orbit coupling of the EuO$_X$ in the 3+ state; while bands centered at around 1125 and 1155 eV correspond to divalent Eu^{2+} 3$d_{5/2}$ and 3$d_{3/2}$ doublet, respectively. Finally, a small band observed at 1143 eV is related to the satellite peak of the Eu^{2+} 3$d_{5/2}$ main peak structure [15, 30, 39, 40]. XPS spectra demonstrate that europium is present in both oxidation states (Eu^{2+} and Eu^{3+}) in all the nanostructures. The elemental sample compositions were evaluated using the integrated areas of the core-level peaks O 1s, C 1s, Eu 3d, and Si 2p after subtraction of the background and fitting the experimental curve. Then, the atomic percentage of one element in the sample was calculated using the relation:
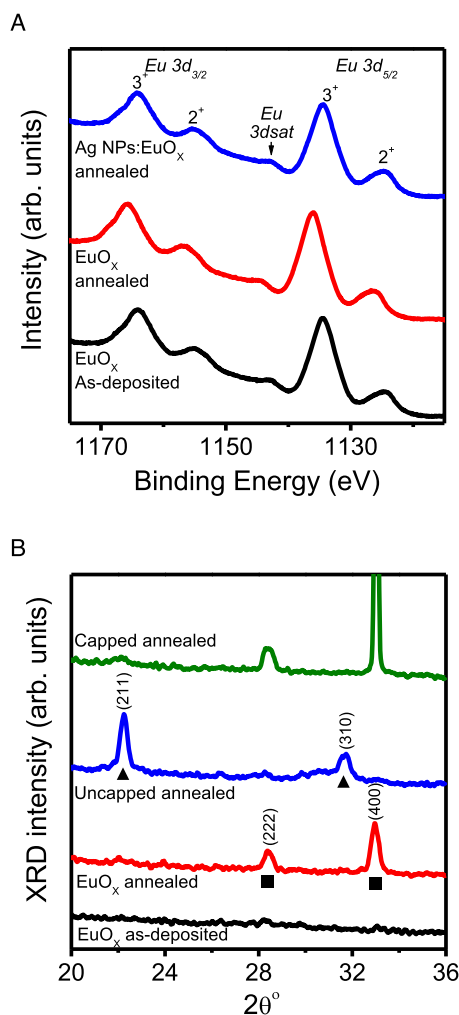

Figure 3: (A) XPS Eu 3d core level spectra of as-deposited and annealed EuO$_X$ references, and annealed uncapped Ag NPs:EuO$_X$ Pl-L hybrid nanostructures. (B) XRD spectra of as-deposited and annealed EuO$_X$ references, and capped and uncapped annealed Ag NPs:EuO$_X$ Pl-L hybrid nanostructures. Annealing temperature = 300 °C. Monoclinic (▲) and cubic (■) crystalline planes are indicated in the figure.

Table 1: Eu^{2+} and Eu^{3+} contents in at%, and Eu^{2+}/Eu$_{total}$ concentration ratios in the EuO$_x$ references (before and after annealing) and uncapped Ag NPs: EuO$_x$ Pl-L hybrid nanostructures (after annealing) determined from XPS measurements.

Sample	T$_{ann}$ [°C]	Eu^{2+} [at%]	Eu^{3+} [at %]	Eu^{2+}/Eu$_{total}$
EuO$_x$	As-deposited	11.24	24.05	0.32
EuO$_x$	300 °C	10.51	22.31	0.32
Ag NPs:EuO$_x$	300 °C	10.76	23.84	0.31

$$Xi = \frac{Ai/Si}{\sum_i Ai/Si}.100 \qquad (1)$$

where Ai is the area of the peak related to atom i, and Si is the reported sensitivity factor of atom i [41]. In the case of Eu, we assumed a similar contribution of the cross-section for the 3d core level of Eu^{3+} and Eu^{2+} peaks [39, 42], and we considered Ai as the sum of the areas under the curves that peaked at 1135 and 1164 eV for Eu^{3+}, while the Eu^{2+} percentage was determined from the areas under the curves corresponding to the Eu^{2+} and peaked at 1125 and 1155 eV. The calculated Eu contents and the Eu^{2+} fraction is shown in Table 1.

The results obtained show that thermal annealing in air up to 300 °C does not affect the relative content of Eu^{2+}, neither does the inclusion of Ag NPs. The Eu^{2+}/Eu$_{total}$ ratio (Eu$_{total}$ = Eu^{2+} + Eu^{3+}) is close to 0.3 in all cases. Thus, both as-deposited and annealed nanostructures, present a layer composed of a mixture of europium oxides, with a majority content of the sesquioxide (Eu$_2$O$_3$) and a lower but significative presence of the monoxide (EuO). The fact that step-annealing in air up to 300 °C (annealing at 300 °C from now on) does not modifies the relative Eu^{2+} content suggests that the presence of Eu^{2+} in the films is due to a partial reduction process during film deposition by PLD. EuO$_x$ layers were produced from a stoichiometric Eu$_2$O$_3$ target in vacuum. Under these experimental conditions, most oxides present an oxygen deficiency caused by the differences in the expansion dynamics of the ablated species present in the laser-generated plasma. Heavy species, such as Eu atoms and ions show a much narrower angular distribution than the much lighter oxygen atoms and ions, which leads to oxygen-deficient films when the substrate is placed in front of the target as it is the case in the present work [31, 43, 44].

Post-deposition thermal step-annealing in air does not alter the Eu^{2+}/Eu^{3+} ratio in the nanostructures; but it induces their crystallization, as is shown in Figure 3B where we present the X-ray diffraction patterns measured for the as-deposited and annealed at 300 °C EuO$_x$ references. The as-deposited EuO$_x$ reference is clearly amorphous,

whereas after step-annealing it presents two peaks at 28.5° and 33.15° that correspond to the Eu$_2$O$_3$ cubic phase (PDF 00-034-0392) [18, 45]. Figure 3B also shows the XRD diffraction patterns for both uncapped and capped Ag NPs:EuO$_x$ Pl-L hybrid nanostructures annealed at 300 °C. They present diffraction peaks that correspond to Eu$_2$O$_3$ with a crystalline phase that depends on the sample configuration. In the case of uncapped nanostructures, the Eu$_2$O$_3$ crystallizes in the monoclinic phase (PDF 00-034-0072) [18, 45] as indicated by the two main peaks located at 22° and in the 31–32° range of its XRD spectrum, while the addition of a capping a-Al$_2$O$_3$ layer favors the crystallization of the Eu$_2$O$_3$ cubic phase. No evidence of the crystallization of any EuO phase (PDF 00-018-0507) [31, 45] was found in any sample.

We have finally calculated the grain size (D) and lattice strain (S) of the EuO$_x$ layers through the Debye–Scherrer equation ($D = 0.93 \lambda/\beta \cos \theta$), and expression ($S \tan \theta = (\lambda/D \cos \theta) - \beta$), respectively [30, 32], where D is the crystalline grain size, λ corresponds to the incident X-ray wavelength (1.54 Å in the case of Cu $K\alpha$ radiation), θ is the Bragg angle of the individual peak, and $\beta = (\beta_{obs} - \beta_{std})$ is obtained after subtracting the instrumental line broadening ($\beta_{std.}$) that is 0.0035 (in 2θ units), to the full width half maxima (FWHM) of the relevant diffraction peak ($\beta_{obs.}$). Table 2 summarizes the data obtained from the XRD analysis of the EuO$_x$ references, and the uncapped and capped nanostructures annealed at 300 °C. The results presented in Figure 3B indicate that the presence of the Ag NPs layer does not determine the crystalline phase of the EuO$_x$ layer; but this is rather related to the deposition of buffer and capping a-Al$_2$O$_3$ layers, since, as discussed in a previous work [18], they induce changes in the stress of the EuO$_x$ layer during crystallization. When only one of them is deposited, EuO$_x$ crystallizes in the monoclinic phase, while when both buffer and capping layers are deposited, EuO$_x$ crystallizes in the cubic phase and, in this case, there is a dominant crystalline orientation along the (400) direction, with a larger nanocrystallite size and reduced strain, which is expected to affect the PL response of the nanostructured films [6, 18, 46].

## 3.2 Optical characterization of Ag NPs:EuO$_x$ Pl-L hybrid nanostructures

Figure 4A Shows the s-polarized (R_s) and p-polarized (R_p) specular reflectance spectra measured for the uncapped Ag NPs:EuO$_x$ nanostructure shown in Figure 1E and F. R_s shows a broad maximum centered at $\lambda \approx 520$ nm and a marked shoulder at $\lambda \approx 380$ nm, while in the case of R_p the

Table 2: Position (2θ) and FWHM of the XRD diffraction peaks, identified crystalline phase and orientation, crystallite size (*D*) and lattice strain (*S*) for each diffraction peak corresponding to the EuO$_x$ reference and the uncapped and capped Ag NPs:EuO$_x$ Pl-L hybrid nanostructures.

Sample	Configuration	2θ	FWHM [2θ]	Phase & orientation	*D* [nm]	*S* [×10^{-3}]
EuO$_x$	–	28.41	0.43	Cubic (222)	21.44	2.10
EuO$_x$	–	32.96	0.41	Cubic (400)	22.82	2.05
Ag NPs:EuO$_x$	Uncapped	22.26	0.35	Monoclinic (202)	26.58	2.31
Ag NPs: EuO$_x$	Uncapped	31.74	0.52	Monoclinic (310)	17.59	2.24
Ag NPs:EuO$_x$	Capped	28.41	0.48	Cubic (222)	19.03	1.66
Ag NPs: EuO$_x$	Capped	33.02	0.18	Cubic (400)	59.01	0.64

broad maximum downshifts to $\lambda \approx 500$ nm, and a second narrow peak appears at $\lambda \approx 370$ nm. We can relate this behavior to the morphology of Ag NPs. As it has been shown in Section 3.1 and Supplementary Material S1, the Ag NPs are not spheres, but oblate ellipsoids. Moreover, since they are randomly oriented in the plane of the nanostructures (Figure S1), they behave optically as oblate spheroids having an in-plane average dimension ($D \approx 9.2 \pm 4.5$ nm) and an NP height $H \approx 5.5 \pm 1.5$ nm, i.e. with an aspect ratio, $H/D < 1$. Figure 4B illustrates the electric field direction for each polarization component of

the incident beam light at an AOI of 55° with respect to the nanostructure surface in the experimental configuration used in the reflectance spectroscopy measurements. When the beam is s-polarized, the electron clouds of the NPs are excited and oscillate along the axes parallel to the substrate (x, y) due to the excitation of transverse plasmons. On the contrary, when the incident beam is p-polarized, the excitation has two components parallel and perpendicular to the substrate. Then, the electron clouds oscillate not only along x and y axes but they do it as well along the axis perpendicular to the substrate (z) and thus, an additional
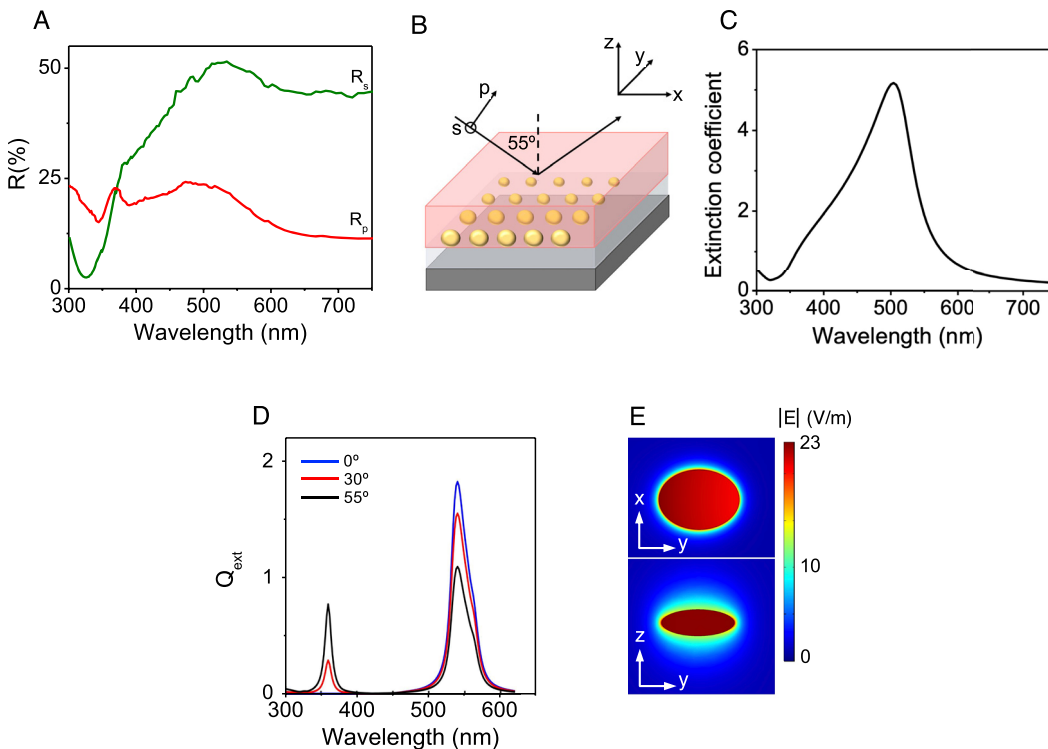
Figure 4: (A) Specular reflectance spectra for s- (R$_s$) and p- (R$_p$) polarized light measured for an uncapped annealed Ag NPs:EuO$_x$ Pl-L hybrid nanostructure at an AOI of 55°. (B) Configuration of the specular reflectance measurements. (C) Effective extinction coefficient spectrum obtained from the simultaneous best fit of R$_s$ and R$_p$ using the procedure described in section S3 of the Supplementary Material. (D) Extinction efficiency (Q$_{ext}$) spectra at increasing angles of incidence calculated using the FEM model described in section S4 of the Supplementary Material for an oblate Ag NP (in-plane long and short axes equal to 10.9 and 7.6 nm, respectively; height = 3.5 nm) embedded in EuO$_x$. (E) Calculated top (top panel) and lateral (bottom panel) view intensity maps of the electric field scattered by the Ag NP upon excitation with a plane wave at $\lambda = 355$ nm and at an incidence angle of 30°.

longitudinal plasmon mode is excited [47, 48]. If NPs are spherical, transverse and longitudinal plasmon modes are degenerate and a single plasmon resonance is observed. However, when the NPs are distorted, the spherical symmetry is broken and the SPR band splits into transverse and longitudinal modes [47, 48]. Thus, in the present case and for p-polarized light the SPR band splits into transverse and longitudinal modes corresponding to electron cloud oscillation in the plane of the nanostructures and perpendicular to it, respectively. Since $H/D < 1$ the transverse resonance shifts into the red, while the longitudinal one shifts to the blue, with respect to the case of spherical NPs, which leads to the two bands at 500 nm and at 370 nm observed in the R_p reflectivity spectrum shown in Figure 4A.

To obtain the extinction spectrum of the uncapped hybrid nanostructure, we modeled it as a layered structure in which the Ag NPs layer is represented by an effective medium approximation. Details on the model and the simulation are included the Supplementary Material S3. We have obtained from the fitting of R_p and R_s the effective refractive index ($N_\mathrm{eff} = n_\mathrm{eff} + i k_\mathrm{eff}$) of the layer containing the Ag NPs. Figure 4C shows the effective extinction coefficient (k_eff). It shows a maximum at 505 nm that corresponds to the transverse SPR mode, and an additional band in the 350–400 nm range that we attribute to the longitudinal SPR mode of the Ag NPs. We have cross-checked this behavior by performing finite element calculation simulations using the COMSOL Multiphysics software [49]. Details about these simulations are given in Section S4 of the Supplementary Material. The structure simulated consists of an oblate Ag NP that is embedded in EuO$_x$. Details on the NP dimensions are given in Section S4 of the Supplementary Material. Figure 4D shows the calculated extinction efficiency Q_ext spectra at increasing angles of incidence with respect to the Ag NP equatorial plane (xy) for a Ag NP having long and short axes equal to 10.9 and 7.6 nm, respectively, and a height of 3.5 nm. At normal incidence, we only observe the transverse modes at $\lambda \approx 540$ nm, while as the AOI increases, a second extinction band at $\lambda \approx 360$ nm appears, which corresponds to the excitation of the longitudinal mode of the Ag NPs [47]. The larger the AOI the more intense the Q_ext corresponding to the resonance of the longitudinal mode. Moreover, since we are considering a single NP with an elliptical in-plane section we appreciate in Figure 4D a shoulder at the long-wavelength side of the transverse mode that corresponds to the breaking of the degeneration of the transverse modes.

We have evaluated the intensity map of the electric field scattered by the Ag NP upon excitation with an incident plane wave at the PL excitation wavelength ($\lambda = 355$ nm) for an incidence angle of 30° with respect to the

Ag NP equatorial plane (xy), which taking into account the Snell law it corresponds to an experimental AOI close to 55° with respect to the surface of the hybrid nanostructures (Figure 4B). The results of the modeling are shown in Figure 4E. The map shows a strong intensification (~×10) of the field intensity along the direction normal (z) to the equatorial plane of the NP (Figure 4E bottom panel). Finally, even if the model used only provides a qualitative interpretation, we have evaluated the effect of the size dispersion of the Ag NPs and the interparticle distance has on the optical response of the nanostructures (details of the modeling are given in Section S4 of the Supplementary Material). The results of these simulations show a broadening of the extinction bands due to the wide distribution of NPs sizes, and a strong increase of the near electric field intensity around the NPs that is about one order of magnitude higher than incident electric field due to the proximity of other NPs. The results of these simulations thus confirm that the optical response of the Ag NPs layer in the conditions of PL experiments is undoubtedly beneficial for the excitation of rare earth ions by increasing their excitation probability [19, 21–23].

3.3 Photoluminescence of Ag NPs:EuO$_X$ Pl-L hybrid nanostructures

All the Pl-L hybrid nanostructures show clear PL emission when excited at 355 nm. Figure 5A compares the PL spectra obtained for uncapped Pl-L hybrid nanostructures having a 30 nm thick EuO$_X$ layer, as a function of the annealing temperature. Spectra were normalized by the maximum PL emission intensity value, obtained at 612 nm for the EuO$_X$ reference annealed at 300 °C (Supplementary Material S5). The PL spectra of EuO$_X$ and Ag NPs:Al$_2$O$_3$ references annealed at 300 °C have been included in the figure for comparison. The EuO$_X$ reference shows the characteristic Eu^{3+} $4f$ intra-transitions emission bands centered at 580 and 612 nm that correspond to the $^5D_0 \rightarrow {}^7F_J$ (J = 0, 1, 2) Eu^{3+} transitions [18–20]. The presence of the Ag NPs has a dramatic impact on the PL response of the nanostructures. As-deposited Pl-L hybrid nanostructures show a broad visible emission band in the 400–660 nm spectral range in addition to the characteristic Eu^{3+} $4f$ intra-transitions emission bands in the 570–640 nm range. The increase of the step-annealing temperature induces a clear increase of the broad VIS band, whereas the Eu^{3+} related emission does not show a significant intensity increase. The overall maximum PL emission intensity was obtained for samples annealed at 300 °C.
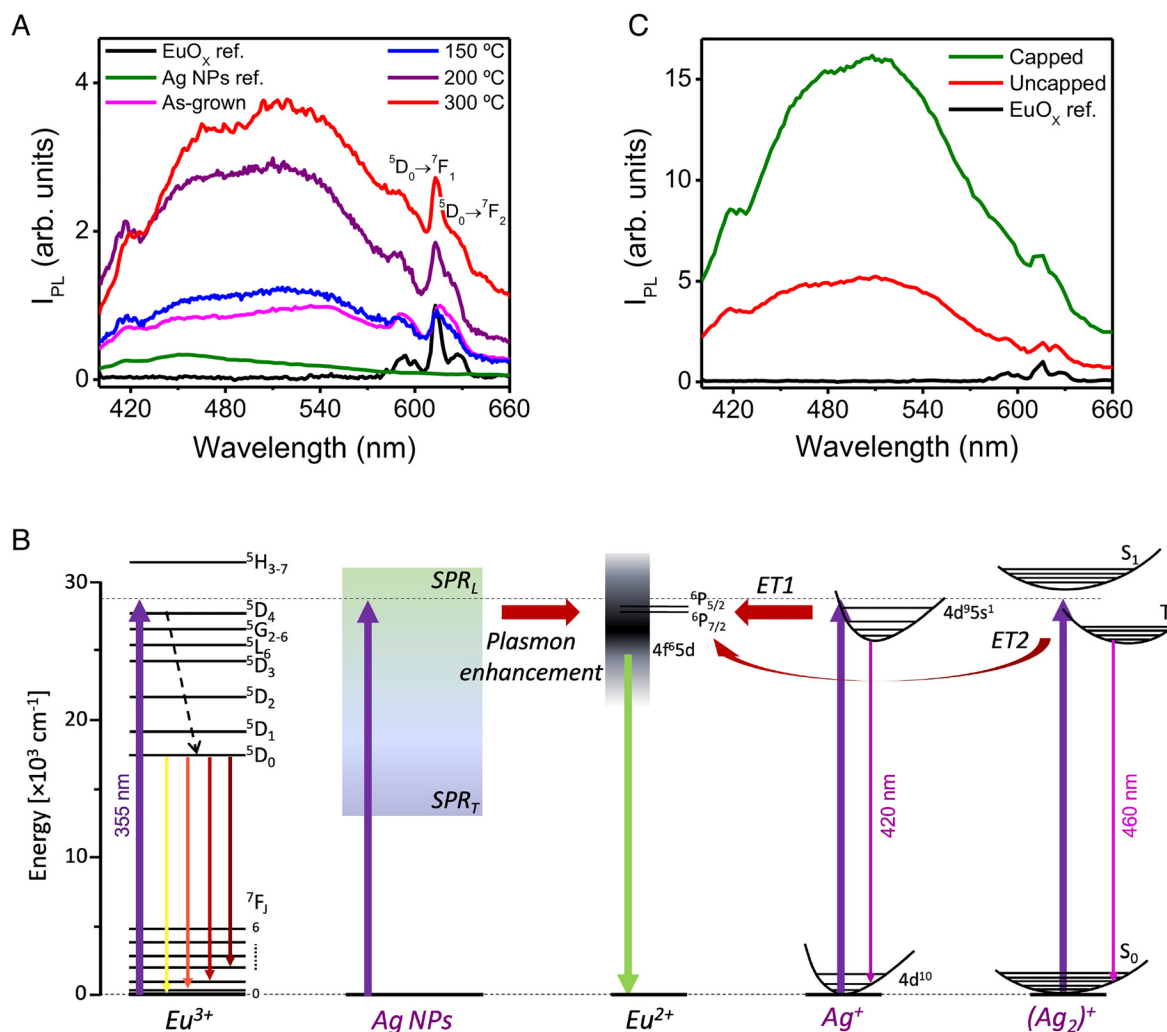
Figure 5: (A) Annealing temperature dependence of the photoluminescence emission spectra from uncapped Ag NPs:EuO$_X$ Pl-L hybrid nanostructures annealed at (red) 300 °C, (purple) 200 °C, (blue) 150 °C, and (magenta) as-grown. PL spectra from EuO$_X$ (black) and Ag NPs:Al$_2$O$_3$ (green) references annealed at 300 °C have been included for comparison. Data are normalized to the PL emission intensity value at 612 nm of the EuO$_X$ reference (λ_{exc} = 355 nm; P = 145 mW). (B) Schematic energy levels of Eu^{3+}, Eu^{2+} and Ag species under 355 nm excitation with possible mechanisms of interaction between Ag species and Eu ions: Energy transfer from Ag$^+$ ions (ET1) and Ag$^+$–Ag^0 pairs (ET2) to Eu^{2+} ions, and plasmonic near-field enhancement associated to the longitudinal dipolar mode of Ag NPs (Plasmon enhancement). (C) PL emission spectra of (red) uncapped and (green) capped Ag NPs:EuO$_X$ Pl-L hybrid nanostructures annealed at 300 °C, and (black) EuO$_X$ reference. Data are normalized to the PL emission intensity value at 612 nm of the EuOX reference annealed at 300 °C. (λ_{exc} = 355 nm; P = 145 mW).

There are many examples that point out the beneficial effect of co-doping with Ag to achieve an intense and broad PL in the case of Europium-doped bulk glasses and crystals [19, 22–26]. In these works, the increase of Eu^{3+} emission is related to ET processes between Ag species and Eu^{3+}, whereas there is controversy about the origin of the broad VIS emission band that is attributed to both the emission of Eu^{2+} ions and different Ag species, such as ions, pairs (Ag$^+$– Ag$^+$, Ag$^+$–Ag^0), small molecule-like Ag clusters not showing SPR (Ag NCs) or Ag NPs. In these cases, nucleation and growth of Ag NPs or NCs and the incorporation of Eu ions to specific sites take place during the synthesis process, which leads to a homogeneous distribution of Ag and Eu dopants.

However, nucleation and growth are completely different in the present case. The different layers (buffer and capping a-Al$_2$O$_3$, Ag NPs, and EuO$_X$) composing the Ag NPs:EuO$_X$ Pl-L hybrid nanostructures were deposited sequentially as independent layers, while the low-temperature annealing limits the possibility of Ag diffusion, which leads to a layered nanostructure with the Ag NPs showing a bidimensional organization in a single layer [23, 29] that is covered by a EuO$_X$ layer, as it is shown in Figure 1F.

In order to gain insight about the origin of the broad VIS emission band, that we will see it renders a chromatic coordinate in the blue-green close to white emission chromatic coordinates, we have compared the spectral

shape of the PL emission of Ag NPs:EuO$_X$ Pl-L hybrid nanostructures with that of the Ag NPs:Al$_2$O$_3$ reference (Figure 5A and Supplementary Material S6). In absence of Ag NPs we observe PL emission from Eu^{3+} but not from Eu^{2+} [18–20], while PL emission from the Ag NPs:Al$_2$O$_3$ reference (Figure 5A) is weak and centered around 450 nm with a tail that extends up to 600 nm. Instead, PL emission intensity of the uncapped Ag NPs:EuO$_X$ nanostructures is much more intense in the whole VIS range and, as it is shown in Figure 5A, it presents a characteristic broad band centered at 520 nm that is not observed in the case of the Ag NPs:Al$_2$O$_3$ reference, along with two shoulders at 420 nm and in the 430–480 nm wavelength range (Supplementary Material S6) that could be related to Ag species [19, 25, 26]. However, since Ag NPs layers in the Ag NPs:Al$_2$O$_3$ reference and in the Pl-L hybrid nanostructures were produced using the same procedure, nonplasmonic Ag species (ions, pairs, and Ag NCs) should be present along with Ag NPs in both cases and, therefore, if the intense VIS emission was related to them, the Ag NPs:Al$_2$O$_3$ reference should show this feature too. Thus, even if from the results shown in Figure 5A and Supplementary Material S6 we cannot completely rule out a limited contribution in the 410–480 nm spectral range from Ag$^+$ ions and Ag$^+$–Ag^0 pairs [19, 25, 26], which can be present in nanostructured films produced by PLD [34], we attribute the broad VIS PL emission in the 400–570 nm range to Eu^{2+} ions, that is triggered by the presence of Ag species. Moreover, the increase of PL emission with the thickness of the EuO$_X$ layer (Figure S10) supports that the broad VIS emission band is related to the EuO$_X$ layer as it is discussed in Supplementary Material S7. Finally, we relate the observed increase of the PL emission intensity upon thermal annealing to two factors. First, the reduction of defects in the EuO$_X$ layer, characteristics of oxide films deposited by PLD, which could cause quenching of the PL emission in the as-deposited nanostructures, and second to the crystallization of the nanostructures (Figure 3B) that orders the local environment around Eu ions [17, 20].

The fact that EuO$_X$ references do not show PL emission from Eu^{2+} (Figure 5A), although ~30% of the europium present in these films is in its +2 sate (Table 1), suggests that either Eu^{2+} is not efficiently excited in absence of Ag NPs, even if both Eu^{3+} and Eu^{2+} ions can absorb the incident laser radiation at 355 nm [9, 15], or Eu^{2+} de-excites non-radiatively from the $4f^6$ $5d$ excited levels. Since Eu^{2+} emission is observed when Ag NPs are introduced into the nanostructures, a nonefficient direct excitation of Eu^{2+} ions in absence of Ag species is most likely to occur and suggests the existence of cooperative excitation processes between Ag species and Eu ions. There are several

excitation and transfer mechanisms that could be responsible for the efficient excitation of Eu^{2+} ions. Figure 5B summarizes the schematic energy levels diagrams of Eu^{3+}, Eu^{2+} ions, and Ag species, along with possible ET channels.

The results presented in Figure 5A and Supplementary Material S6 suggested the presence of Ag$^+$ and Ag$^+$–Ag^0 pairs. Ag ions and pairs absorb the excitation wavelength at 355 nm, and they can partially transfer the excitation to Eu ions through ET mechanisms [19, 24, 25]. However, as shown in Figure 2B these species would be confined at the a-Al$_2$O$_3$/EuO$_X$ interface, which would limit the impact of ET on the VIS PL enhancement due to the small excitation distance range associated with the ET processes. The second mechanism that could be responsible for the PL enhancement is the excitation of Eu ions due to the intensification of the local field associated with the SPR of the Ag NPs [19, 22, 23], which requires that the SPR band overlaps with the absorption bands of the Eu ions. The AOI of the 355 nm excitation laser beam used in the PL experiments was 55° (Figure 4B). Under these experimental conditions, our hybrid nanostructures present an absorption shoulder in the 350–400 spectral range associated with the resonance of the longitudinal mode of Ag NPs surface plasmons (Figure 4C) as it has been discussed in Section 3.2. This enables the absorption of the 355 nm incident beam and thus, induces the enhancement of the near electromagnetic field in the vicinity of the Ag NPs as it has been shown in Figure 4E. The estimated Ag NPs surface coverage is close to 40%, with the EuO$_X$ layer being deposited on and in-between the Ag NPs (Figure 1F). This implies that there is a large surface area in which Eu ions and Ag NPs are in close contact. Moreover, the coupling distance for an efficient transfer of excitation from Ag NPs to Eu ions can be as long as 30 nm (see Supplementary Material S7) [23]. Thus, we consider that SPR-mediated excitation rather than ET from Ag$^+$ and Ag$^+$–Ag^0 pairs to Eu ions, is the most likely excitation path for Eu ions in the present case. The fact that Eu^{3+} emission does not show an evident increase in the presence of Ag species when compared to that of Eu^{2+} ions, could be related to the different character of Eu^{2+} and Eu^{3+} transitions: while $5d \rightarrow 4f$ Eu^{2+} transitions are spin and parity allowed, $4f \rightarrow 4f$ Eu^{3+} transitions are forbidden, and thus the former is much more intense than the latter, which could mask the increase of Eu^{3+} emission [11, 20].

We have finally, analyzed the effect that the configuration of the nanostructures has on the PL response, as it is known to affect the relative intensity of the Eu^{3+} PL emission bands [18, 46], and the presence of a capping layer determines the crystalline structure of the Ag NPs:EuO$_X$ nanostructures (Figure 3B). Figure 5C compares the PL emission spectra of uncapped and capped Pl-L hybrid nanostructures annealed at 300 °C. We observe a strong
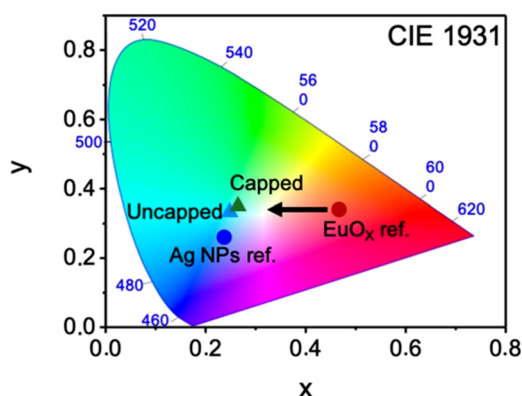
Figure 6: CIE 1931 chromatic diagram corresponding to the (●) EuO$_X$ and (●) Ag NPs:Al$_2$O$_3$ references, and the (▲) uncapped and (▲) capped Ag NPs:EuO$_X$ Pl-L hybrid nanostructures.

increase of the overall PL intensity emission for a similar EuO$_X$ active layer in the case of the capped nanostructures. We have evaluated the contribution of Eu^{2+} and Eu^{3+} to the PL emission intensity increase and spectral shape change. As it is described in detail in Supplementary Material S6, PL emission of both Eu^{2+} and Eu^{3+} increases when adding the capping layer. However, the contribution of Eu^{+3} ions to the total PL emission is only a few %, which makes difficult to evaluate its relative increase, yet we have estimated that the relative increase of PL emission from both Eu^{2+} and Eu^{3+} ions is similar ($\approx \times 3$). Concerning the spectral shape of PL emission, we observe that Eu^{3+} emission (Figure S9B) reflects the change of the nanocrystalline phase from monoclinic to cubic when adding the capping layer. However, this change does not affect the overall spectral shape of nanostructures emission due to the small contribution of Eu^{3+} ions to the total emission. Instead, this is dominated by Eu^{2+} PL. As it is shown in Figure S9C, the overall shape in the case of uncapped and capped nanostructures is similar, the main difference being the decrease of the relative intensity of the PL band at $\lambda \approx$ 420 nm when adding the capping layer that could be related to the change of the crystalline phase. Therefore, we consider that the main effect of the capping layer is to increase the overall PL emission intensity, while the shape of the PL emission is only slightly affected. This behavior is likely related to the beneficial effect of the capping a-Al$_2$O$_3$ layer, since it leads to denser EuO$_X$ films [18], with larger crystallites and reduced strain (Figure 3B and Table 2), and it protects EuO$_X$ active layers from the incorporation of OH$^-$ groups from the atmosphere [50], thus decreasing non-radiative de-excitation paths in the case of capped nanostructures.

To conclude, we have evaluated the chromatic coordinates (CIE 1931) of the Pl-L hybrid nanostructures and the references. The results are shown in Figure 6. The coordinates of the EuO$_X$ reference are clearly in the red region (x = 0.46, y = 0.34), whereas that of the Ag NPs reference fall into the blue region (x = 0.23, y = 0.25). Finally the inclusion of the Ag NPs into the EuO$_X$ layer induces a shift toward the light blue-green region: (x = 0.25, y = 0.33) and (x = 0.26, y = 0.35) for uncapped and capped Ag NPs:EuO$_X$ Pl-L hybrid nanostructures annealed at 300 °C, respectively. Therefore, the addition of the capping layer allows fine tuning of PL emission, and the color coordinates of Ag NPs:EuO$_X$ nanostructures are very close to the pure white CIE 1931 chromatic coordinates (x = 0.33, y = 0.33).

4 Conclusions

Hybrid plasmonic-luminescent Ag NPs:EuO$_X$ nanostructures have been produced in a single step by PLD in vacuum at room temperature. Ag NPs show a bidimensional organization in a single layer, while EuO$_X$ fills in the spacing between the NPs as well as covers them. XPS analysis shows that Eu is present in the nanostructures in both oxidation states: Eu^{2+} ($\approx$30%) and Eu^{3+} ($\approx$70%). Annealing in air at a moderate temperature (300 °C) does not significantly alter the morphology of the Ag NPs array neither modify the Eu^{2+}/Eu^{3+} ratio, but it induces the formation of Eu$_2$O$_3$ nanocrystallites and leads to an increase of the PL response. The presence of the Ag species has a strong impact on the PL response. Without Ag NPs, EuO$_X$ references present the characteristic red emission related to the intra 4f transitions of Eu^{3+} ions, while no contribution from Eu^{2+} ions is observed. Instead, the presence of Ag NPs leads to an intense emission in the blue-green visible spectral region that is related to the $4f^6\,5d^1 \rightarrow 4f^7$ transitions of Eu^{2+}. These densely packed Ag NPs optically behave as oblate spheroids, that in the PL experimental configuration used present an absorption band associated to their surface plasmon longitudinal mode, which overlaps with the 355 nm excitation wavelength used. The coupling of nearby NPs contributes to enhance this absorption. This allows efficient excitation of Eu^{2+} ions by SPR mediated excitation. Finally, the presence of a capping a-Al$_2$O$_3$ enhances the PL response of the Ag NPs:EuO$_X$ Pl-L hybrid nanostructures due to the improvement of their nanocrystalline structure. These EuO$_X$-based nanostructures are of great interest for the development of compact and integrable WL-LEDs due to their broad visible emission that is close to pure white emission, and the possibility of controlling selectively the Eu^{2+}/Eu^{3+} excitation ratio through the deposition parameters, which allows tuning their color emission.

References

[1] R. J. Xie and N. Hirosaki, "Silicon-based oxynitride and nitride phosphors for white LEDs-a review," *Sci. Technol. Adv. Mater.*, vol. 8, pp. 588–600, 2007.

[2] K. Li, M. Shang, H. Lian, and J. Lin, "Recent development in phosphors with different emitting colors via energy transfer," *J. Mater. Chem. C*, vol. 4, pp. 5507–5529, 2016.

[3] H. Terraschke and C. Wickleder, "UV, blue, green, yellow, red, and small: newest developments on Eu^{2+}-doped nanophosphors," *Chem. Rev.*, vol. 115, pp. 11352–11378, 2015.

[4] X. Qin, X. Liu, W. Huang, M. Bettinelli, and X. Liu, "Lanthanide-activated phosphors based on 4*f*–5*d* optical transitions: theoretical and experimental aspects," *Chem. Rev.*, vol. 117, pp. 4488–4527, 2017.

[5] J. Qiao, J. Zhao, Q. Liu, and Z. Xia, "Recent advances in solid-state LED phosphors with thermally stable luminescence," *J. Rare Earths*, vol. 37, pp. 565–572, 2019.

[6] A. Tiwari and S. J. Dhoble, "Tunable lanthanide/transition metal ion-doped novel phosphors for possible application in w-LEDs: a review," *Luminescence*, vol. 35, pp. 4–33, 2020.

[7] T. Zhong and P. Goldner, "Emerging rare-earth doped material platforms for quantum nanophotonics," *Nanophotonics*, vol. 8, pp. 2003–2015, 2019.

[8] A. Vaskina, R. Kolkowskia, A. F. Koenderinka, and I. Staude, "Light-emitting metasurfaces," *Nanophotonics*, vol. 8, pp. 1151–1198, 2019.

[9] G. Bellocchi, G. Franzò, M. Miritello, and F. Iacona, "White light emission from Eu-doped SiOC films," *Appl. Phys. Express*, vol. 7, 2014, Art. no. 012601.

[10] R. Gautier, X. Li, Z. Xia, and F. Massuyeau, "Two-step design of a single-doped white phosphor with high color rendering," *J. Am. Chem. Soc.*, vol. 139, pp. 1436–36, 2017.

[11] W. B. Dai, "Mechanism of the reduction and energy transfer between Eu^{2+} and Eu^{3+} in Eu-doped CaAl$_2$Si$_2$O$_8$ materials prepared in air," *J. Mater. Chem. C*, vol. 2, pp. 3951–3959, 2014.

[12] P. Dang, D. Liu, G. Li, et al., "Mixing the valence control of Eu^{2+}/Eu^{3+} and energy transfer construction of Eu^{2+}/Mn^{2+} in the solid solution (1–*x*)Ca$_3$(PO$_4$)$_2$–xCa$_9$Y(PO$_4$)$_7$ for multichannel photoluminescence tuning," *Inorg. Chem. Front.*, vol. 6, pp. 2837–2849, 2019.

[13] J. A. C. Santana, J. M. An, N. Wu, et al., "Effect of gadolinium doping on the electronic band structure of europium oxide," *Phys. Rev. B*, vol. 85, 2012, Art. no. 014406.

[14] D. V. Averyanov, C. G. Karateeva, I. A. Karateev, et al., "Atomic-scale engineering of abrupt interface for direct spin contact of ferromagnetic semiconductor with silicon," *Sci. Rep.*, vol. 6, 2016, Art. no. 22481.

[15] A. Mariscal-Jimenez, A. T. Martín-Luengo, B. Galiana, et al., "Photoluminescence and stoichiometry correlation in nanocrystalline EuO$_x$ thin films: tunable color emission," *J. Phys. Chem. C*, vol. 124, pp. 15434–15439, 2020.

[16] P. Chen, Y. Mao, Sh. Hou, et al., "Effects of In$_2$O$_3$ nanoparticles doping on the photoluminescent properties of Eu^{2+}/Eu^{3+} ions in silica glasses," *Ceram. Int.*, vol. 45, pp. 233–238, 2019.

[17] I. Camps, A. Mariscal, and R. Serna, "Preparation and broadband white emission of Eu-doped thin films based on SiAlON," *J. Lumin.*, vol. 191, pp. 97–101, 2017.

[18] A. Mariscal, A. Quesada, I. Camps, F. J. Palomares, J. F. Fernández, and R. Serna, "Tuning Eu^{3+} emission in europium sesquioxide films by changing the crystalline phase," *Appl. Surf. Sci.*, vol. 374, pp. 71–76, 2016.

[19] I. I Kindrat, B. V. Padlyak, B. Kukliński, A. Drzewiecki, and V. T. Adamiv, "Enhancement of the Eu^{3+} luminescence in Li$_2$B$_4$O$_7$ glasses co-doped with Eu, and Ag," *J. Lumin.*, vol. 204, pp. 122–129, 2018.

[20] G. Bellocchi, G. Franzò, F. Iacona, et al., "Eu^{3+} reduction and efficient light emission in Eu$_2$O$_3$ films deposited on Si substrates," *Opt. Express*, vol. 20, pp. 5501–5507, 2012.

[21] Q. Liu, Y. Tian, W. Tang, X. Jing, J. Zhang, and S. Xu, "Comprehensive studies of the Ag$^+$ effect on borosilicate glass ceramics containing Ag nanoparticles and Er-doped hexagonal NaYF$_4$ nanocrystals: morphology, structure, and 2.7 μm emission," *Nanophotonics*, vol. 7, pp. 913–923, 2018.

[22] O. L. Malta, P. A. Santa-Cruz, G. F. De Sá, and F. Auzel, "Fluorescence enhancement induced by the presence of small silver particles in Eu^{3+} doped materials," *J. Lumin.*, vol. 33, pp. 261–272, 1985.

[23] A. Pillonnet, A. Berthelot, A. Pereira, et al., "Coupling distance between Eu^{3+} emitters and Ag nanoparticles," *Appl. Phys. Lett.*, vol. 100, 2012, Art. no. 153115.

[24] M. Eichelbaum and K. Rademann, "Plasmonic enhancement or energy transfer? On the luminescence of gold-, silver-, and lanthanide-doped silicate glasses and its potential for light-emitting devices," *Adv. Funct. Mater.*, vol. 19, pp. 2045–2052, 2009.

[25] M. Sandrini, R. F. Muniz, V. S. Zanuto, et al., "Enhanced and tunable white light emission from Ag nanoclusters and Eu^{3+}-co-doped CaBAl glasses," *RSC Adv.*, vol. 8, pp. 35263–35270, 2018.

[26] J. A. Jimenez, S. Lysenko, and H. Liu, "Enhanced UV-excited luminescence of europium ions in silver/tin-doped glass," *J. Lumin.*, vol. 128, pp. 831–833, 2008.

[27] E. Soria, G. Baraldi, M. Martinez-Orts, J. Toudert, R. Serna, and J. Gonzalo, "Conformal covering and optical response of pulsed laser deposited bidimensional Ag nanoparticle arrays," *Appl. Surf. Sci.*, vol. 473, pp. 442–448, 2019.

[28] J. Gonzalo, D. Babonneau, C. N. Afonso, and J. P. Barnes, "Optical response of mixed Ag–Cu nanocrystals produced by pulsed laser deposition," *J. Appl. Phys.*, vol. 96, pp. 5163–5168, 2004.

[29] X. Wang, R. Morea, J. Gonzalo, and B. Palpant, "Coupling localised plasmonic and photonic modes tailors and boosts ultrafast light modulation by gold nanoparticles," *Nano Lett.*, vol. 15, pp. 2633–2639, 2015.

[30] S. Kumar, R. Prakash, R. J. Choudhary, and D. M. Phase, "Resonant photoemission spectroscopic studies of Eu$_2$O$_3$ thin film," *J. Appl. Phys.*, vol. 120, 2016, Art. no. 125309.

[31] J. N. Beukers, J. E. Kleibeuker, G. Koster, et al., "Epitaxial EuO thin films by pulsed laser deposition monitored by in situ x-ray photoelectron spectroscopy," *Thin Solid Films*, vol. 518, pp. 5173–5176, 2010.

[32] A. Mariscal, A. Quesada, A. T. Martín-Luengo, et al., "Europium monoxide nanocrystalline thin films with high near-infrared transparency," *Appl. Surf. Sci.*, vol. 456, pp. 980–984, 2018.

[33] G. Baraldi, M. Carrada, J. Toudert, et al., "Preventing the degradation of Ag nanoparticles using an ultrathin a-Al2O3 layer as protective barrier," *J. Phys. Chem. C*, vol. 117, pp. 9431–9439, 2013.

[34] J.-P. Barnes, A. K. Petford-Long, R. C. Doole, et al., "Structural studies of Ag nanocrystals embedded in amorphous Al$_2$O$_3$ grown by pulsed laser deposition," *Nanotechnology*, vol. 13, pp. 465–470, 2002.

[35] S. A. Little, T. Begou, R. W. Collins, and S. Marsillac, "Optical detection of melting point depression for silver nanoparticles via in situ real time spectroscopic ellipsometry," *Appl. Phys. Lett.*, vol. 100, 2012, Art. no. 051107.

[36] V. M. Samsonova, N. Y. Sdobnyakova, V. S. Myasnichenkoa, et al., "A comparative analysis of the size dependence of the melting and crystallization temperatures in silver nanoparticles via the molecular dynamics and Monte-Carlo methods," *J. Surf. Investig: X-ray Synchrotron Neutron Tech.*, vol. 12, pp. 1206–1209, 2018.

[37] G. Albrecht, M. Ubl, S. Kaiser, H. Giessen, and M. Hentschel, "Comprehensive study of plasmonic materials in the visible and near-infrared: linear, refractory, and nonlinear optical properties," *ACS Photonics*, vol. 5, pp. 1058–1067, 2018.

[38] X. Li, T. Sasaki, C. Grezes, D. Wu, et al., "Predictive materials design of magnetic random-access memory based on nanoscale atomic structure and element distribution," *Nano Lett.*, vol. 19, pp. 8621–8629, 2019.

[39] C. Caspers, M. Muller, A. Gray, et al., "Chemical stability of the magnetic oxide EuO directly on silicon observed by hard X-ray photoemission spectroscopy," *Phys. Rev. B*, vol. 84, 2011, Art. no. 205217.

[40] T. K. Pietrzak, A. Gołębiewska, J. Płachta, et al., "Photoluminescence of partially reduced Eu^{2+}/Eu^{3+} active centers in a NaF–Al$_2$O$_3$–P$_2$O$_5$ glassy matrix with tunable smooth spectra," *J. Lumin.*, vol. 208, pp. 322–326, 2019.

[41] C. D. Wagner, L. E. Davis, M. V. Zeller, J. A. Taylor, R. M. Raymond, and L. H. Gale, "Empirical atomic sensitivity factors for quantitative analysis by electron spectroscopy for chemical Analysis," *Surf. Interface Anal.*, vol. 3, pp. 211–225, 1981.

[42] L. A. Zavala-Sanchez, G. A. Hirata, E. Novitskaya, K. Karandikar, M. Herrera, and O. A. Graeve, "Distribution of Eu^{2+} and Eu^{3+} ions in hydroxyapatite: a cathodoluminescence and Raman study," *ACS Biomater. Sci. Eng.*, vol. 1, pp. 1306–1313, 2015.

[43] J. A. Chaos, J. Gonzalo, C. N. Afonso, J. Perrière, and M. T. García-González, "Growth of stoichiometric and textured LiNbO$_3$ films on Si by pulsed laser deposition," *Appl. Phys. A*, vol. 72, pp. 705–710, 2001.

[44] R. Perez-Casero, J. Perrière, A. Gutierrez-Llorente, et al., "Thin films of oxygen-deficient perovskite phases by pulsed-laser ablation of strontium titanate," *Phys. Rev. B*, vol. 75, 2007, Art. no. 165317.

[45] S. Gates-Rector and T. Blanton, "The powder diffraction file: A quality materials characterization database," *Powder Diffr.*, vol. 34, pp. 352–360, 2019.

[46] R. Stefan, L. C. Bolundut, L. Pop, G. Borodi, E. Culea, and P. Pascuta, "Copper nanoparticles enhanced luminescence of Eu^{3+} doped lead tellurite glass ceramics," *J. Non-Cryst. Solids*, vol. 505, pp. 9–17, 2019.

[47] J. Margueritat, J. Gonzalo, C. N. Afonso, et al., "From silver nanolentils to nanocolumns: surface plasmon–polaritons and confined acoustic vibrations," *Appl. Phys. A*, vol. 89, pp. 369–372, 2007.

[48] I. O. Sosa, C. Noguez, and R. G. Barrera, "Optical properties of metal nanoparticles with arbitrary shapes," *J. Phys. Chem. B*, vol. 107, pp. 6269–6275, 2003.

[49] A. Cuadrado, J. Alda, and F. J. González, "Multiphysics simulation for the optimization of optical nanoantennas working as distributed bolometers in the infrared," *J. Nanophotonics*, vol. 7, 2013, Art. no. 073093.

[50] M. Irannejad, G. Jose, P. Steenson, and A. Jha, "Enhancement in optical and microstructure properties of Er^{3+}-doped phospho-tellurite glass thin film," *Opt. Mater.*, vol. 34, pp. 1272–1276, 2012.